Remote plasma-assisted oxidation of SiC: a low temperature process for SiC–SiO_2 interface formation that eliminates interfacial Si oxycarbide transition regions

2004 J. Phys.: Condens. Matter 16 S1815

(http://iopscience.iop.org/0953-8984/16/17/018)

INSTITUTE OF PHYSICS PUBLISHING JOURNAL OF PHYSICS: CONDENSED MATTER

J. Phys.: Condens. Matter **16** (2004) S1815–S1837 PII: S0953-8984(04)65080-6

Remote plasma-assisted oxidation of SiC: a low temperature process for SiC–SiO_2 interface formation that eliminates interfacial Si oxycarbide transition regions

Gerald Lucovsky and Hiro Niimi[1]

Department of Physics, North Carolina State University, Raleigh, NC 2795-8202, USA

E-mail: lucovsky@unity.ncsu.edu and gerry_lucovsky@ncsu.edu

Received 23 June 2003
Published 16 April 2004
Online at stacks.iop.org/JPhysCM/16/S1815
DOI: 10.1088/0953-8984/16/17/018

Abstract

Remote plasma-assisted oxidation of SiC is a low temperature process, 300 °C, for the formation of device quality interfaces on SiC. This paper discusses two aspects of the process: (i) the motivation for eliminating high temperature oxidation processes that can generate silicon oxycarbide, Si–O–C, interfacial regions which can be a source of interfacial defects and (ii) the kinetics of the remote plasma-assisted oxidation process that effectively eliminates interfacial Si oxycarbide transition regions. The differences between interfacial relaxation at Si–SiO_2 and SiC–SiO_2 are based on the relative stabilities of the suboxides of Si and SiC, SiO_x and (Si, C)O_x, respectively.

1. Introduction

The attainment of a low defect density gate oxide on SiC substrates is critically important in optimizing the electrical performance of field effect transistor devices. In particular, the interface between the substrate and the gate oxide plays a key role in determining transistor performance characteristics and reliability. The first section of this paper focuses on interfacial bonding Si–O–C arrangements that have been identified at SiC–SiO_2 interfaces formed by high-temperature thermal oxidation processes. This is put in perspective by first considering bonding at device quality Si–SiO_2 interfaces.

Studies based on x-ray photoelectron spectroscopy, XPS, of Si–SiO_2 interfaces prior to post-oxidation annealing have identified an interfacial compositional transition layer within 0.5 nm of the interface which contains intermediate oxidation states of Si, Si^{+1}, Si^{+2} and Si^{+3}, or equivalently Si suboxide (SiO_x, $x < 2$) interfacial transition regions [1–3]. These

[1] Present address: Silicon Technology Research, Texas Instruments, Dallas, TX 75243, USA.

0953-8984/04/171815+23$30.00

transition regions can contribute to interface roughness and also give rise to electronically active defects. Improvement of device properties is typically achieved integrating a post-oxidation anneal [4]. Analysis of interface bonding chemistry and structure has shown that the improvements after annealing derive from reductions of suboxide bonding groups in interfacial transition regions, effectively smoothing the Si–SiO_2 interface [4–13]. Studies of SiC–SiO_2 interfaces have also identified an interfacial compositional transition layer [14–16]. Depending on the substrate polytype, oxidation temperature and ambient, wet versus dry, results have shown that carbon atoms may become trapped in the growing oxide as they diffuse out away from the growth interface, forming an oxycarbide interface layer. For example, Hornetz *et al* [14] have shown using angle-resolved XPS that a thin Si oxycarbide layer $\sim$1 nm exists at the SiC–SiO_2 interface and that graphite may be present on the top surface of the oxide. Using Auger electron spectroscopy (AES) Chaudhry [15] reported carbon incorporation in wet oxides grown on 3C-SiC as high as 14 at.% and that dry oxides contained much more silicon than stoichiometric SiO_2, i.e. suboxide bonding, indicating that wet and dry oxidation differ considerably in mechanisms for 3C-SiC. The effect of carbon in the oxide non-stoichiometric suboxide transition regions on the electrical performance of SiC metal-oxide–semiconductor (MOS) field effect transistor devices is unknown. Transistor characteristics following various post-oxidation annealing treatments have been reported by Lipkin and Palmour [17], with improvements being noted in interface trap density and electron mobility. The effect of these post-oxidation anneals, however, is not well understood microscopically. Therefore, a fundamental understanding of the bonding environment when carbon is incorporated into the oxide and its effect on suboxide formation is needed, especially in light of

(i) the numerous SiC substrate polytypes,
(ii) the speculation regarding oxidation mechanisms [18] and
(iii) room temperature channel electron mobility values which are substantially lower than those measured in the bulk [17].

This section of the paper extends studies of the thermal stability of plasma-deposited SiO_x thin films [19–21] to suboxides of Si and C, defined here as (Si, C)O_x. The research identifies changes in structure and bonding using Fourier transform infrared spectroscopy (FTIR) Raman scattering and high-resolution transmission electron microscopy (HRTEM) as a function of rapid thermal annealing (RTA) temperatures that are of importance for understanding changes in interface bonding and chemistry occurring during the thermal oxidation of SiC and subsequent annealing of the SiC–SiO_2 interfaces. In particular, a Si–O–C bonding group is identified to form in films annealed between 900 and 1000 °C in an inert environment, and subsequently disappear after annealing at 1050 °C. The results of this research then provide important information underpinning SiC device processing technology.

The second section of the paper presents a low temperature remote plasma-assisted oxidation process for forming SiC–SiO_2 interfaces. As noted above, there is considerable interest in SiC for high temperature device applications, including power transistors. To fabricate these devices, it will be necessary to gain an increased understanding of the chemical bonding at the SiC–SiO_2 interface, and in particular to develop processing that minimizes interfacial defects and transition regions, and maximizes device reliability as manifested in reductions in the rate of interfacial and bulk defect generation during operation. It has been established that the oxide that forms on SiC during high temperature oxidation in O_2 ambients is SiO_2 and that this oxidation process can yield SiC–SiO_2 interfaces and gate dielectrics with sufficiently low defect densities for field effect transistor (FET) operation [17]. However, channel mobilities at room temperature in depletion mode FETs are significantly lower than expected from bulk SiC properties and much research has been focused on explaining these

differences and improving channel mobilities [22]. Since SiO_2 is the dominant solid state oxidation product, oxidation products involving carbon atoms must include gaseous molecules such as CO; as oxide growth progresses these must be transported from the buried growth interface through the oxide and out of the film. However, as noted above, this does not preclude the formation of additional interfacial carbon atom bonding arrangements, such as Si–C and C–O, as have been reported in silicon oxycarbide transition regions [14]. The molar volume mismatch between SiC and SiO_2 is greater than the corresponding mismatch between Si and SiO_2, so that intrinsic levels of strain at SiC–SiO_2 interfaces are anticipated to be at least as high as the values of approximately $3–5 \times 10^9$ dyn cm^{-2} reported in Si–SiO_2 [23]. This section of the paper deals with an alternative low temperature method for semiconductor–dielectric interface formation that has been successfully applied to crystalline Si device technology [24, 25]. As applied to Si, this approach provides independent control of Si–SiO_2 interface formation and dielectric film growth. The Si–SiO_2 interface and a superficially thin oxide layer ∼0.5 nm thick are formed by a low temperature, 300 °C, remote plasma-assisted oxidation (RPAO) process and the remainder of the oxide layer is deposited by a low temperature, 300 °C, remote plasma-enhanced chemical vapour deposition (RPECVD) process. Device quality interfaces are obtained by subjecting the plasma-processed Si–SiO_2 heterostructure to a post-deposition RTA, e.g. in an inert ambient such as Ar for 30 s at 900 °C. The 900 °C anneal promotes both chemical and structural interface relaxations, including a minimization of interfacial suboxide bonding arrangements in transition regions between the Si crystal and the stoichiometric bulk oxide [26]. A similar plasma-assisted process has recently been applied to SiC and has yielded SiC–SiO_2 interfaces with defect state densities comparable to what has been achieved on SiC by conventional high temperature thermal oxidation [27]. The potential advantages of this two-step approach to SiC–SiO_2 interface formation are:

(i) it reduces the requirement for transporting gaseous reaction products, such as CO molecules, away from the interface as the oxide grows; and
(ii) it can also reduce strain-induced interface defect generation, since only a small fraction of the total oxide layer thickness is generated by consumption of the SiC substrate.

The focal point of this portion of the paper is a study of SiC–SiO_2 interface formation by RPAO using on-line AES to monitor interface bonding chemistry and the initial oxide growth rate. Before discussing the SiC AES measurements, it is useful to summarize the results of device studies on vicinal Si and SiC wafers using the plasma-assisted processing steps identified above. Studies by Bjorkman *et al* [28] demonstrated that densities of mid-gap defect states (D_{it}) as low as $\sim 3 \times 10^{10}$ cm^{-2} eV^{-1} could be obtained on Si(111) surfaces by using conventional thermal oxidation, metal electrodes and 400 °C post metal anneals (PMA) in an H_2-containing ambient. Previous studies had always shown higher values for Si(111) as compared to the Si(100) surfaces used in the integrated circuit wafers (see [9]). Studies performed by Yasuda *et al* [29] on p-type Si(111) vicinal wafers up to 5° off-axis in the $11\bar{2}$ direction showed that the density of mid-gap states (D_{it}) increased by relatively small amounts from $\sim 3 \times 10^{10}$ cm^{-2} eV^{-1} to about 6×10^{10} cm^{-2} eV^{-1} as the vicinal angle increased up to about 5°. The studies of Yasuda *et al* were on Si–SiO_2 structures prepared by the same two-step RPAO–RPECVD 300 °C process that has been described above and is discussed in detail in [5]. Al electrodes were employed and a 400 °C PMA in a H_2-containing ambient was used. The magnitudes of the incremental increases in D_{it} with increasing vicinal angle indicated that only a relatively small fraction of the dangling bond states at the step edges contributed to increases in D_{it} with increasing step edge density due to increasing the vicinal angle.

At the present state of the art, the highest quality SiC crystals for devices are epitaxial layers formed on Si-atom-terminated 6H SiC vicinal wafers approximately 3.5° off-axis in the

$11\bar{2}0$ direction. Using RPAO–RPECVD, the results of device studies using vicinal 6H p-type SiC as reported by Goelz *et al* [26] are markedly different than the results reported for vicinal Si. MOS capacitors were prepared by essentially the same two-step RPAO–RPECVD process as used by Yasuda *et al* [24] for Si. However, following a conventional PMA in an H_2-containing ambient, D_{it} values were in excess of 10^{13} cm^{-2} eV^{-1}, even when an 1150 °C furnace anneal in Ar was interposed between the oxide film deposition and the metallization steps. However, if the high temperature anneal was performed in an H_2-containing ambient then D_{it} values after the conventional 40 °C PMA were reduced significantly into the 10^{11} cm^{-2} eV^{-1} range [27]. This large difference in defect densities is approximately equal to the number of carbon atom dangling bonds at the step edges, suggesting that these carbon atom dangling bonds were not H-terminated after a conventional 400 °C PMA but instead required the higher temperature exposure to H for termination. It is important to note that interfaces prepared on the same type of vicinal SiC surfaces by conventional high temperature thermal oxidation processes also required a high temperature anneal in an H_2-containing ambient to yield values of D_{it} in the 10^{11} cm^{-2} eV^{-1} range [29]. Step edge carbon atom dangling bonds on vicinal Si wafers can either be terminated by oxygen atoms that connect to the SiO_2 dielectric, or by hydrogen atoms. The annealing results in [27] and [29] are consistent with hydrogen atom termination of step edge carbon atom dangling bonds, i.e. dangling bond elimination would be accomplished by atomic hydrogen generated during the 1150 °C anneal. To study interfacial bonding arrangements between SiC and SiO_2, on-line AES has been used to monitor the initial stages of SiC–SiO_2 interface formation. This same approach has been used to study the initial stages of interface formation on Si by both RPAO and rapid thermal oxidation (RTO) and using both O_2 and N_2O oxygen atom source gases [26]. This paper extends this approach to SiC and focuses on the initial stages of the RPAO process as applied to both flat or vicinal SiC surfaces using O_2 source gases. Some preliminary results are also presented for RPAO using N_2O as the oxygen atom source gas. The local bonding arrangements at the step edges of the vicinal 6H SiC wafers is presented. Results of AES studies of SiC RPAO include comparisons between the RPAO of SiC and Si. Detailed results are presented for RPAO using O_2 and preliminary results for RPAO using N_2O. Finally, the major results of this RPAO study are discussed with an emphasis on

(i) the results of the on-line AES studies and
(ii) the passivation of step edge dangling bonds as revealed by charge reductions in D_{it} levels as determined from electrical measurements.

2. Chemical and phase stability of amorphous silicon oxycarbides

2.1. Sample preparation and characterization

Thin films of hydrogenated $SiCO_x$, approximately 200 nm thick, were deposited on fused silica and high resistivity, ∼5 Ω cm, p-type Si wafers in an ultrahigh vacuum (UHV) compatible, multi-chamber system using a RPECVD process, as described elsewhere [30]. Fused silica substrates were used for Raman studies to eliminate spectral interference from a crystalline-Si substrate peak. For FTIR analysis, high resistivity Si wafers were used to minimize free-carrier absorption in the substrate. The wafers were also single-side polished and 'orange peel' roughened on the other side to minimize multiple reflections in the substrate and reduce background interference fringes. Prior to sample insertion into the load lock of the deposition system, (i) a 15 s HF rinse ∼50:1, followed by (ii) a 1 min deionized water rinse and (iii) a dry nitrogen *blow dry* were performed on the Si wafers. A 10 min ultrasonic bath in a sulfuric/chromic acid glass cleaning solution followed by (i) a 10 min deionized water rinse

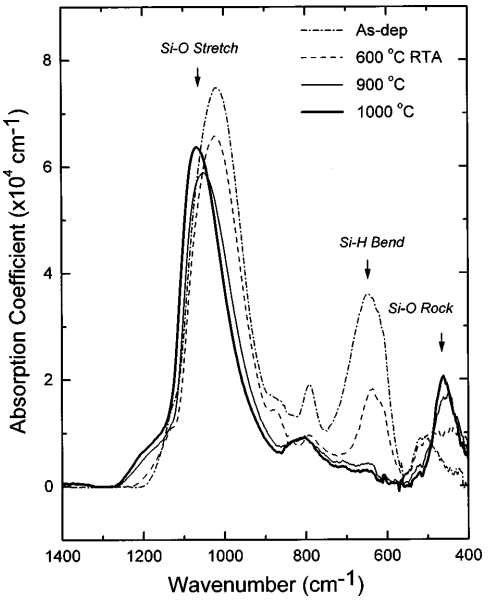

Figure 1. FTIR absorption spectra of SiO_x ($x \sim 0.15$) thin films before and after annealing.

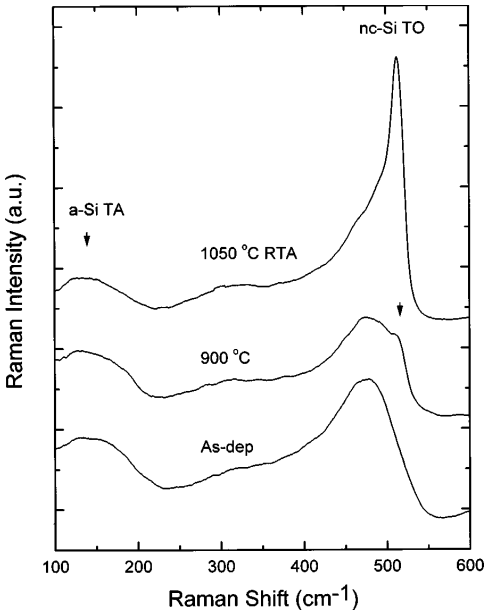

Figure 2. Raman scattering spectra of SiO_x ($x \sim 0.15$) thin films before and after annealing.

and (ii) a dry nitrogen blow dry was performed on the fused silica. Films of (Si, C)O_x were deposited at 250 °C and 300 mTorr using (i) excited neutral species, e.g. O^{2*} and O atoms, transported out of an upstream He/O_2 radio-frequency plasma (13.56 MHz) and (ii) downstream injected SiH_4/CH_4 mixtures [23]. Alloy compositions for the films were determined by XPS and Rutherford backscattering (RBS). The composition of the ∼(Si, C)O_x films was $x \sim 0.15$ and C ∼ 10 at.%, with an uncertainty of ∼0.02 at.%. For baseline reference and comparisons, thin films of hydrogenated SiO_x, $x \sim 0.15$ and SiC_x, $x \sim 0.2$, were also prepared by similar RPECVD processes. As-deposited these films contained significant amounts of bonded hydrogen, ∼10 at.%. The local bonding environments and structure in these alloy films was studied using a combination of FTIR, Raman and HRTEM, as a function of RTA temperatures between 600 and 1100 °C. Characterization was performed before and after annealing to the desired temperature at a ramp rate of 100 °C s^{-1} in 1 atm Ar for 90 s.

For FTIR analysis, spectra were subtracted from a reference Si wafer. An Ar^+ laser operating at 514.53 nm, with incident laser power on the sample of approximately 150 mW, was used for Raman scattering analysis. HRTEM imaging was performed on cross-sectional samples, prepared using standard cutting and polishing techniques, in the bright-field mode with an accelerating voltage of 250 kV.

2.2. Experimental results

2.2.1. SiO_x baseline studies. Figure 1 shows FTIR absorption spectra before and after annealing to various temperatures for SiO_x ($x \sim 0.15$) thin films [31]. Three distinct spectral features are noted and shift upon annealing. The peak of 630 cm^{-1} is a Si–H bending mode [32] and is a result of hydrogen incorporation, ∼15 at.%, into the growing film from the source gas SiH_4. Upon annealing to temperatures greater than about 800 °C this feature completely disappears, demonstrating that the initial reaction upon annealing to temperatures of about

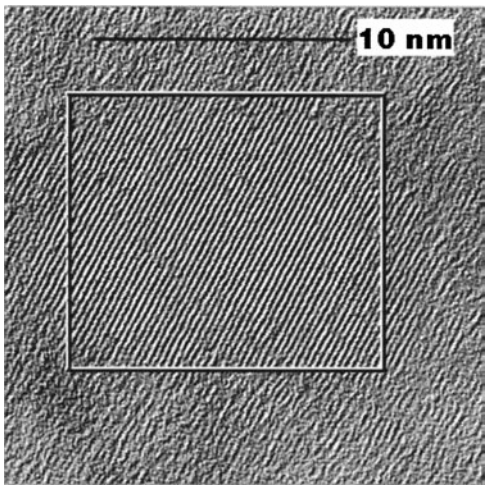

Figure 3. HRTEM image of a SiO_x ($x \sim 0.15$) thin film after annealing to 900 °C.

600 °C involves the loss of bonded hydrogen to silicon from the films. The decrease in the infrared peak at 630 cm^{-1} is accompanied by a similar decrease in a coupled Si–O–Si–H vibration at 780 cm^{-1} [32]. Once hydrogen is lost, this feature is replaced by a Si–O bond bending mode at ∼810 cm^{-1}. The very strong peak in between 1015–1080 cm^{-1} is the Si–O bond stretching mode [32]. In the as-deposited films, this Si–O stretching mode is located at ∼1017 cm^{-1}, indicative of suboxide bonding arrangements [6, 19, 32]. As the annealing temperature is increased the Si–O stretching mode shifts towards higher frequencies, established that atomic rearrangements are occurring and that suboxide bonding is being reduced. This feature becomes characteristic of stoichiometric and thermally relaxed SiO_2 (see [6, 13]) after annealing to approximately 900 °C. The third distinguishing Si–O feature is the Si–O bond rocking mode located at ∼440 cm^{-1}. This mode becomes pronounced after annealing to approximately 900 °C, and again is characteristic of stoichiometric and thermally relaxed SiO_2.

Figure 2 shows Raman spectra of SiO_x, $x \sim 0.15$, thin films before and after annealing to various temperatures. The spectra for the as-deposited films indicated that they were amorphous and were not compositionally homogeneous. A transverse acoustic phonon mode at 150 cm^{-1} was observed, indicating that amorphous-Si, ∼a-Si, regions were present. The onset of nanocrystalline-Si (nc-Si) formation in these films was observed in the spectra by the emergence of an optical phonon mode at ∼515 cm^{-1}. In figure 2, this feature becomes observable after annealing at 900 °C and is more pronounced after annealing to 1050 °C. Consistent with Raman analysis, figure 3 shows a digitally enhanced HRTEM image of a SiO_x, $x \sim 0.15$, film after annealing to 900 °C. Randomly oriented Si crystallites, as verified through selective area diffraction, were observed to form throughout the films, with their size increasing as the annealing temperature was increased. The size of the crystallites that formed after annealing to 900 °C was approximately 10 nm. The box in figure 3 outlines a typical Si crystallite. In summary, the significant bonding and morphology changes that occur between as-deposited films and films annealed at 900 °C correspond to the formation of stoichiometric and structurally relaxed SiO_2 regions, from FTIR analysis and nanocrystalline-Si regions, from Raman and TEM analysis.

2.2.2. SiC_x baseline studies. Figure 4 shows FTIR spectra before and after RTA to various temperatures for SiC_x ($x \sim 0.2$) thin films. Analysis of the spectra shows that the initial

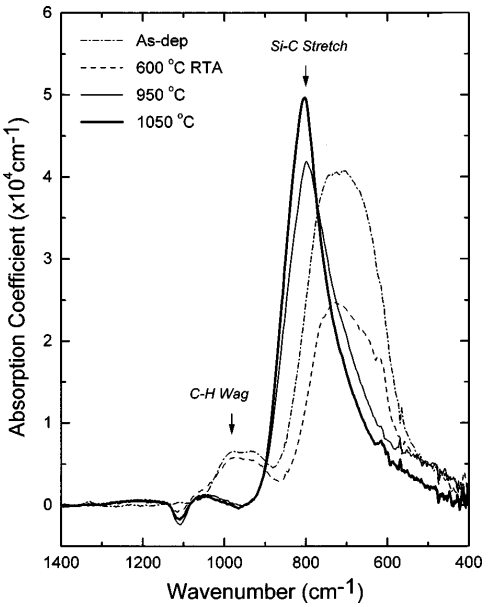

Figure 4. FTIR absorption spectra of SiC_x ($x \sim 0.2$) thin films before and after annealing.

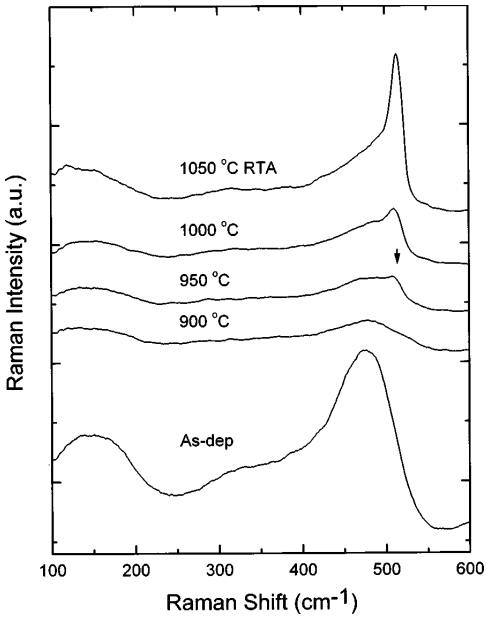

Figure 5. Raman scattering spectra of SiC_x ($x \sim 0.2$) thin films before and after annealing.

reaction involves the loss of hydrogen bonded to silicon and carbon. The modes between 900 and 1000 cm^{-1} are due to C–H bond wagging motions [33] and disappear above 700 °C annealing temperature. The intensity of the Si–H bending mode at 630 cm^{-1} drops sharply after annealing above 800 °C. A Si–CH bond wagging mode [33], which is present in the same vicinity as the Si–H bending mode, and a very weak Si–CH bond bending mode [33] present at about 1340 cm^{-1} both decrease upon annealing to about 800 °C. Most evident in the spectra is the appearance of a relatively narrow Si–C bond stretching mode located at 800 cm^{-1} after annealing to 950 °C. Further increases in annealing temperature shift this mode towards higher frequencies, indicating increased C to Si coordination [34]. Figure 5 shows Raman spectra before and after annealing to various temperatures for SiC_x ($x \sim 0.2$) thin films. The as-deposited films were amorphous and compositionally inhomogeneous, as similarly shown above for the SiO_x films. Also, as in the case for the SiO_x films, Raman spectra of the SiC_x films show that Si crystallization occurs after high temperature annealing. As shown in figure 5, the feature at 515 cm^{-1} represents the formation of nanocrystalline-Si regions and occurs after annealing to approximately 950 °C. Note that no phonon modes of any other crystalline phases such as SiC were observed. For example, for all of the crystalline SiC polytypes, both the transverse and longitudinal optical phonon [35] modes occur at between 780 and 980 cm^{-1} and were not detected. Additionally, neither crystalline nor amorphous carbon–carbon vibrations were detected. HRTEM imaging (not shown) is consistent with these results and, in particular, no crystalline phases other than silicon were observed in the selective area diffraction patterns. In summary, the significant bonding and morphology changes that occur between as-deposited films and films annealed at 950 °C correspond to the formation of chemically ordered a-SiC regions, from FTIR analysis, and nanocrystalline-Si regions, from Raman and TEM analysis.

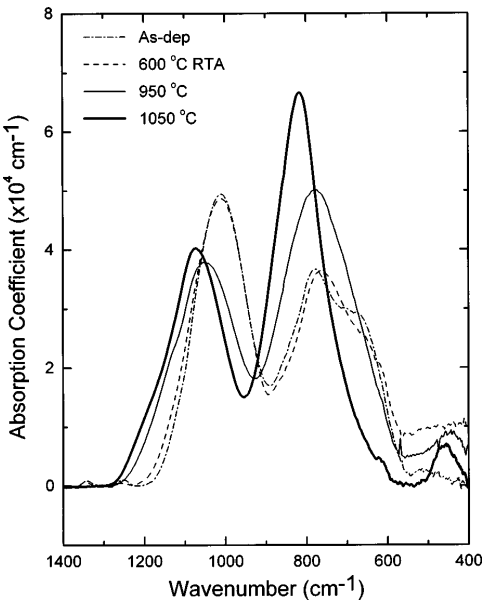

Figure 6. FTIR absorption spectra of (Si, C)O_x ($x \sim 0.15$ and C $\sim$ 10 at.%) thin films before and after annealing.

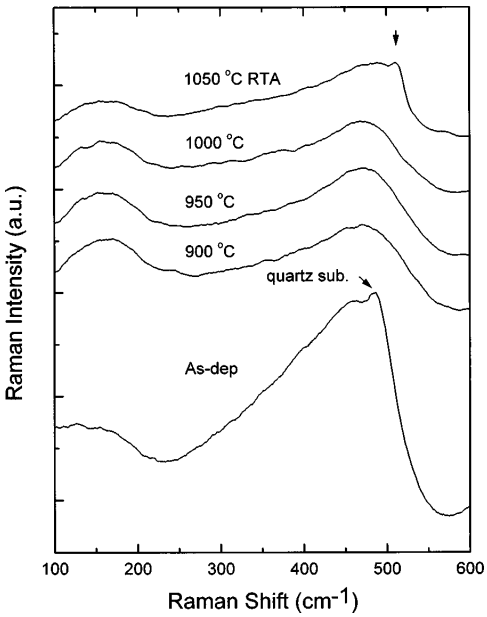

Figure 7. Raman scattering spectra of (Si, C)O_x ($x \sim 0.15$ and C $\sim$ 10 at.%) thin films before and after annealing.

2.2.3. (Si, C)O_x studies. After establishing baseline reference results for SiO_x and SiC_x films, results are now presented for films in which CH_4 has been added to the Si suboxide source gas mix of SiH_4 and O_2 to form (Si, C)O_x alloys. Figure 6 shows FTIR spectra before and after annealing of (Si, C)O_x ($x \sim 0.15$ and C $\sim$10 at.% films. As shown in figure 6, the spectra are essentially a combination of the constituent SiO_x and SiC_x spectra, however with several important and subtle differences. For these films, the initial thermally driven annealing reaction also involved the loss of bonded hydrogen from both Si–H and C–H groups, as explained above for SiC_x films. A well defined Si–C bond stretching mode located at 800 cm^{-1} emerges in the (Si, C)O_x spectra, but after annealing to 1050 °C rather than 950 °C, as in the SiC_x films. Further increases in annealing temperature also shift this mode towards higher frequencies, indicating increased C to Si coordination [34]. Similar to the SiO_x films, in the as-deposited (Si, C)O_x films, the Si–O stretching mode is initially located at 1015 cm^{-1}, indicative of suboxide bonding arrangements. As the annealing temperature is increased the Si–O stretching mode shifts towards higher frequencies, signifying that atomic rearrangement is occurring and that suboxide bonding is being reduced. However, at approximately 900 °C a shoulder located at $\sim$1125 cm^{-1} is observed to form on the high frequency side of the Si–O stretching mode and is attributed to Si–O–C bonding groups [33, 36, 37] on the basis of its frequency relative to the Si–O–Si stretching mode. In the Si–O–C bonding group, oxygen is the bridging atom between Si–O_4 and O–Si–C_3 tetrahedra. This feature is not observed after annealing to 1050 °C, and stoichiometric, thermally relaxed SiO_2 is formed. The implications of this added feature in the spectra will be addressed in section 2.4.

Figure 7 shows Raman spectra before and after annealing of (Si, C), O_x ($x \sim 0.15$ and C $\sim$ 10 at.% films. Again, the films were amorphous and compositionally inhomogeneous, as deduced for the SiO_x and SiC_x films. After annealing to approximately 1050 °C, and as shown in figure 7, a feature at 513 cm^{-1} represents the formation of nanocrystalline-Si regions. As

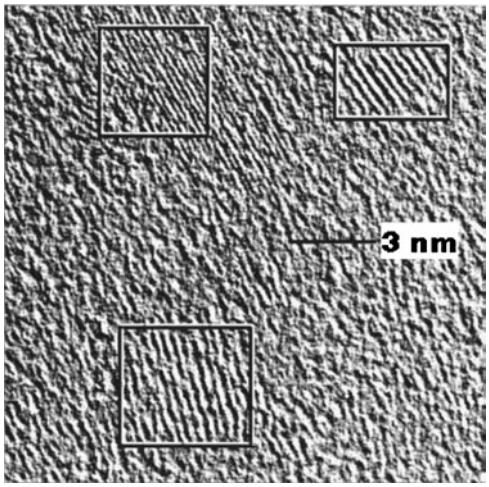

Figure 8. HRTEM image of a (Si, C)O_x ($x \sim 0.15$ and C $\sim$ 10 at.%) thin film after annealing to 1050 °C.

with the SiC_x films, no other phonon modes of crystalline phases were detected, indicating that crystalline regions of SiC or C were not formed. Note that the peak in the as-deposited spectra at 490 cm^{-1} is due to the fused silica substrate. Figure 8 shows a digitally enhanced, HRTEM image of (Si, C)O_x ($x \sim 0.15$ and C $\sim$ 10 at.% films after annealing to 1050 °C. Consistent with Raman analysis, only randomly oriented crystallites of Si were observed to form throughout the films. The size of the crystallites was approximately 4 nm. The boxes in figure 8 outline typical Si crystallites. For annealing temperatures less than 1050 °C, no crystalline products were detected in the TEM image. In summary, the significant bonding and morphology changes that occur between as-deposited films and films annealed at 1050 °C correspond to the formation of stoichiometric, structurally relaxed SiO_2 regions and ordered a-SiC regions, from FTIR analysis, and nanocrystalline-Si regions, from Raman and TEM analysis.

2.3. Discussion of $SiCO_x$ results

To further correlate the trends in the data, and also to elucidate the extra feature in the FTIR spectra of the (Si, C)O_x films that has been attributed to Si–O–C arrangements, the full width at half-maximum (FWHM), $\Delta\nu$, of the Si–O and Si–C bond stretching modes as a function of annealing temperature has been examined. As the FWHM of these modes decreases, the degree of structural ordering is increased. The FWHM of the Si–O bond stretching mode as a function of annealing temperature for the SiO_x and (Si, C)O_x films is therefore plotted in figure 9. The FWHM of the Si–C bond stretching mode for the SiC_x and (Si, C)O_x films as a function of annealing temperature is plotted in figure 10. The size of the data points is the standard deviation in these measurements. As shown in figure 9, $\Delta\nu$ of the Si–O bond stretching mode for the SiO_x films remains essentially constant upon annealing to 800 °C and then begins to decrease after 900 °C. This decrease in $\Delta\nu$ after 900 °C annealing correlates

(i) with the formation of stoichiometric and structurally relaxed SiO_2 as determined by the shift in the Si–O bond stretching peak position (figure 1) and
(ii) with the formation of nanocrystalline-Si regions as determined through Raman spectra and TEM (figures 2 and 3).

In contrast, $\Delta\nu$ of the Si–O bond stretching mode for the (Si, C)O_x films increases significantly upon annealing to 900 °C, remains constant between 900 and 1000 °C and then drops sharply

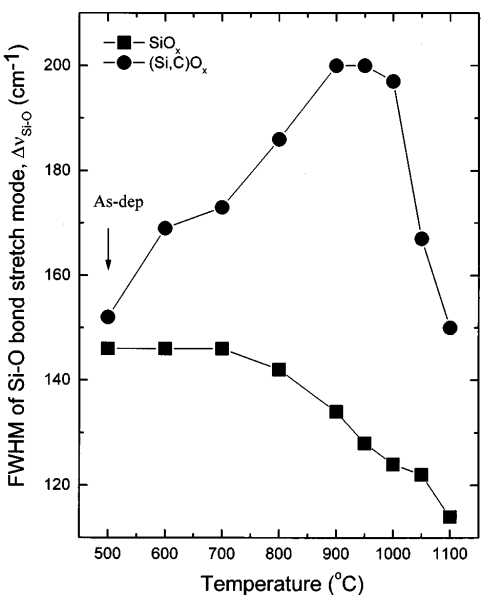

Figure 9. FWHM, $\Delta\nu$, of the Si–O bond stretching mode as a function of annealing temperature for SiO_x ($x \sim 0.15$) and (Si, C)O_x ($x \sim 0.15$ and C $\sim$ 10 at.%) thin films.

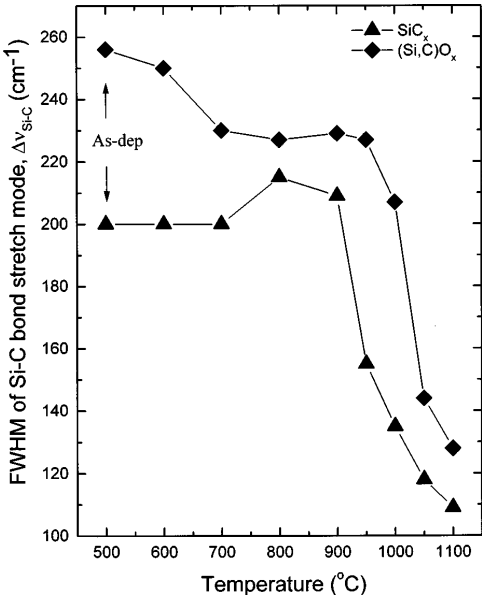

Figure 10. FWHM, $\Delta\nu$, of the Si–C bond stretching mode as a function of annealing temperature for SiC_x ($x \sim 0.2$) and (SiC)O_x ($x \sim 0.15$ and C $\sim$ 10 at.%) thin films.

after annealing to 1050 °C. This trend correlates with results presented above in figures 6–8. As previously mentioned, a shoulder on the high frequency side of the Si–O stretching mode attributed to Si–O–C bonding was observed to emerge in the spectra of figure 6 between annealing temperatures of 900 and 1000 °C, and then *disappear* at 1050 °C. The disappearance of this shoulder after annealing to 1050 °C coincides with

(i) a sharp decrease in $\Delta\nu$ of the Si–O stretch mode in figure 9,
(ii) the formation of stoichiometric and structurally relaxed SiO_2 regions, as determined by the shift in the Si–O bond stretching peak position in figure 6 and
(iii) the formation of nanocrystalline-Si regions as determined through Raman spectra and TEM in figures 7 and 8, respectively.

Figure 10 shows $\Delta\nu$ for the Si–C bond stretching mode in the SiC_x and (Si, C)O_x films as a function of annealing temperature. Once more, the trends correlate with previous results. For the SiC_x films, a sharp decrease in $\Delta\nu$ of the Si–C bond stretching mode occurs after annealing to 950 °C, which coincides with (i) the formation of chemically ordered a-SiC regions in figure 4 and (ii) nanocrystalline-Si regions in figure 5. For the (Si, C)O_x films, a sharp decrease in $\Delta\nu$ of the Si–C bond stretching mode does not occur until after annealing to 1050 °C, which coincides with the elimination of Si–O–C bonding groups. This is also consistent with the formation of (i) stoichiometric, thermally relaxed SiO_2 regions and ordered a-SiC regions in figure 6 and (ii) nanocrystalline-Si regions in figures 7 and 8. Additional quantitative evidence for the elimination of Si–O–C bonding groups in the (Si, C)O_x films upon annealing to 1050 °C is shown in figures 11 and 12. Figure 11 shows only the FTIR spectra of (Si, C)O_x ($x \sim 0.15$) films, C $\sim$ 10 at.%, annealed at 1000 and 1050 °C (compare with figure 6). Figure 12 shows the corresponding first derivative spectra in figure 11. As shown in figure 11, a shoulder is evident at approximately 1125 cm^{-1} after annealing to 1000 °C, and is not present after annealing to

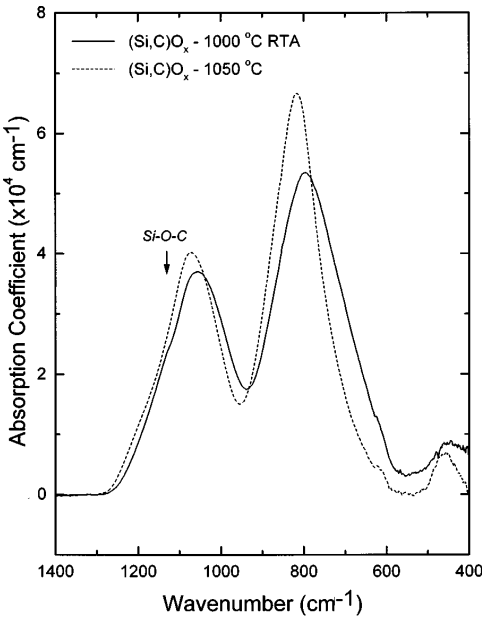

Figure 11. FTIR absorption spectra of (Si, C)O_x ($x \sim 0.15$ and C $\sim$ 10 at.%) thin films after annealing to 1000 and 1050 °C.

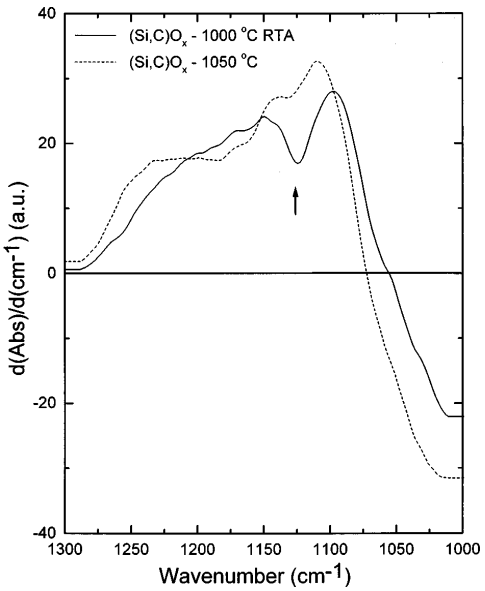

Figure 12. First derivative FTIR absorption spectra of (Si, C)O_x ($x \sim 0.15$ and C $\sim$ 10 at.%) thin films after annealing to 1000 and 1050 °C.

1050 °C. The differentiated spectrum in figure 12 after annealing to 1000 °C shows that the derivative decreases abruptly at 1125 cm^{-1} due to the shoulder on the high frequency side of the Si–O bond stretching mode caused by Si–O–C bonding groups. After annealing to 1050 °C, the shoulder is eliminated in figure 11 and the corresponding derivative spectrum in figure 12 is smooth. We will now discuss how these results on *bulk* films analysed in this study correlate with changes in interface bonding and chemistry observed to occur during the thermal oxidation of SiC and subsequent annealing of SiC–SiO_2 interfaces. Before doing this we will first consider the SiO_x films. Our results showed that at approximately 900 °C suboxide bonding was eliminated and the films separated into stoichiometric, thermally relaxed SiO_2 regions and nanocrystalline-Si regions. These results are in accordance with studies performed directly on Si–SiO_2 interfaces. For example, suboxide bonding at Si–SiO_2 interfaces before and after annealing at 900 °C has been studied by XPS [7, 38, 39], AES [13], TEM [5], difference x-ray diffraction [10] and more recently XPS using monochromatic synchrotron radiation [4]. These studies have confirmed the reduction of excess suboxide bonding by annealing in an inert ambient at 900 °C. In addition, the experiments described in [5] establish that growing an oxide at 900 °C is not equivalent to growth at 900 °C followed by annealing at the same temperature. The apparent saturation of annealing effects in Si–SiO_2 interfaces after 900 °C annealing suggests that the phase separation reaction observed in the deposited SiO_x thin films at 900 °C, i.e. $SiO_x \rightarrow SiO_2$ + nc-Si, also occurs at the crystal interface. However, there are two important differences in the reorganization that take place at the Si–SiO_2 interface. First, the separation is incomplete at the monolayer level, inferring that annealed Si–SiO_2 interfaces have a residual suboxide bonding of the order of a few monolayers. Second, there is no evidence for the formation of nc-Si. The separation reaction results in increased crystallization at the Si–SiO_2 interface, so that in place of the formation of nanocrystallites of Si, Si derived from SiO_x regions is incorporated into the Si substrate.

Now turning to SiC–SiO_2 interfaces, observations based on the occurrence of Si–oxycarbide groups at the interface by XPS [14] and significant improvements in device performance by an oxidation/annealing sequence [17], in which the oxidation is performed at a temperature in excess of 1025 °C and the post-oxidation anneal at 900 °C, are interpreted as follows. Based on the alloy studies presented above, which show that oxycarbide bonding is eliminated at approximately 1050 °C, the requirement for a high temperature oxidation is to remove Si–O–C bonding groups that form at the boundary between Si surface atoms and the growing oxide layer. Since device fabrication is usually done on Si faces of 6H or 4H wafers, the annealing step at 900 °C then presumably performs the same function as at Si–SiO_2 interfaces, reducing suboxide bonding in interfacial transitions regions and smoothing the interface.

Finally, the results presented above on the thermochemical stability of silicon oxycarbide thin films deposited via chemical vapour deposition are in accordance with results in the literature on the characterization of silicon oxycarbide glasses prepared from sol–gel precursors [40, 41].

2.4. Summary for (Si, C)O_x Studies

The thermal stability of silicon–oxygen–carbon alloy thin films (Si, C)O_x has been studied by a combination of FTIR spectroscopy, Raman scattering and HRTEM. Reference films of SiO_x and SiC_x were also prepared and analysed. Results showed that, for the SiO_x films, a structural/chemical transformation takes place at 900 °C in which the films separated into stoichiometric, thermally relaxed SiO_2 and nanocrystalline-Si regions. For the SiC_x films, a structural/chemical transformation takes place at 950 °C in which the films are separated into chemically ordered a-SiC and nanocrystalline-Si regions. In the (Si, C)O_x system, similar structural/chemical transformations take place at 1050 °C, with the film separating into ordered a-SiC regions, stoichiometric, thermally relaxed SiO_2, and nanocrystalline-Si regions. However, a very important difference was noted for the (Si, C)O_x films. At temperatures of 900–1000 °C a Si–O–C bonding group was observed to form that in turn has been assumed to inhibit the phase separation process until the Si–O–C bonding group was dissociated and a C–O group was eliminated at 1050 °C. Important implications of this study for SiC–SiO_2 interface processing are that oxidation must be performed above 1050 °C to ensure minimal Si oxycarbide bonding at the interface and that a 900 °C post-oxidation anneal is necessary to reduce suboxide bonding and smooth the interface.

3. Remote plasma-assisted oxidation of SiC

3.1. Local bonding at step edges

The dangling bond geometry for Si(111) wafers off cut in the $11\bar{2}$ direction has been discussed in [4] and references therein. The steps are effectively two atom layers high and the step edge atoms have a single dangling bond. The steps on 6H SiC with Si-terminated surfaces are more complex due to the larger unit cell. The repeat pattern of 6H SiC extends over 12 atomic planes of alternating Si and C atoms, as shown in figure 13. For off cut angles in the $11\bar{2}0$ direction, the vicinal Si face surfaces can either include two different six-atom steps that are separated by Si-atom-terminated terrace regions, or alternatively consist of six two-atom layer steps/6H repeat pattern. Figure 13 indicates the bonding arrangements for the two different six-atom steps. The first set of steps are in an ABC sequence with one carbon atom dangling bond per double-layer Si–C component, and the second set of steps are an ACB sequence with two carbon atom dangling bonds per double-layer Si–C component. The average number of

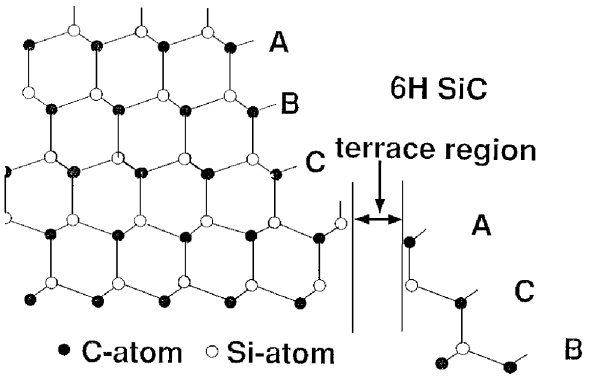

Figure 13. Schematic representation of surface and step bonding for 6H SiC vicinal wafers. The C atom dangling bonds for the first six-atom, three-layer sequence are one per step edge C atom; for the second six-atom, three-layer sequence, there are two dangling bonds per step edge C atom. The six-atom steps are separated by flat terrace regions with Si-atom dangling bonds.

dangling bonds per step in 6H SiC(0001) is 1.5 dangling bonds per step edge atom, whereas in Si(111) off cut in the $11\bar{2}$ direction it is only one dangling bond per step atom. The spacing between single steps on Si(111) off cut in the $11\bar{2}$ direction is 5 nm for a 3.5° off cut angle, so that the ratio of step edge to terrace dangling bonds is approximately 0.06. For a 3.5 off cut angle on SiC, the dangling bond ratio is higher by a factor of 1.5 due to the different step edge terminations of the ABC and ACB sequences. If the 6H SiC surface has two atom steps, as is likely for the wafers used in this study, the dangling bond considerations are the same. Starting with the same ABC sequence as in figure 13, the first three two-atom steps are terminated by C atoms with one dangling, and the second three two-atom steps by C atoms with two dangling bonds. This means that the number of dangling bonds per step on the average is still 1.5 times greater than for off cut Si wafers. For C-terminated SiC faces, the terrace atoms are C and the step edge atoms are Si.

3.2. Experimental results for remote plasma oxidation

The samples used in this study were p-type 6H SiC purchased from Cree Corporation with Si and C faces. Similar to polar faces on III–V compounds, the polar faces on SiC are either Si or C faces. Note further that this particular designation is used independent of any surface contamination. One set of the wafers was oriented on a principal axis, e.g. the (0001) direction, and the other was a vicinal wafer off cut at approximately 3.5° in the $11\bar{2}0$ direction. The surface of the on-axis sample was prepared from a bulk ingot and the surface of the off-axis sample used in these studies was from an epitaxially grown film. The surfaces of the wafers were cleaned following a procedure suggested by Cree Research, Inc. [42]. The *ex situ* cleaning consisted of (i) sequential rinses in trichloroethane (TCE), acetone and methanol, followed by (ii) a conventional two-bath RCA clean. The sacrificial oxide formed in the second step of the RCA clean was removed by rinsing in dilute HF. Samples were then loaded into a multi-chamber system, which provides separate UHV-compatible chambers for RPAO and AES. The experimental procedure was to alternate AES measurements with RPAO processing. A similar approach has been applied to RPAO of Si and, through analysis of the AES data, two kinds of information were obtained: (i) the chemical bonding at the Si–SiO_2 interface and (ii) the oxide thickness as a function of oxidation time [43]. The experimental details are discussed for SiC with Si faces. Following this discussion, the research results are presented for the wafers with

C faces. Figures 14(a) and (b), respectively, give differential AES spectra for flat and vicinal SiC obtained by RPAO using an O_2 source gas. The experimental processing conditions are: (i) a substrate temperature of 300 °C, (ii) a process pressure of 300 mTorr, (iii) a plasma power to the He/O_2 mixture of 30 W and (iv) flow rates of 200 standard cubic centimetres per minute (sccm) of He and 20 sccm and O_2.

The as-loaded samples show surface contamination by oxygen and nitrogen that was not removed by the *ex situ* cleaning process. Since the levels of surface contamination were sub-monolayer, no *in situ* cleaning was attempted. This was in part due to the limited temperature capabilities of the plasma-processing chamber; the substrate heater in this chamber cannot heat a wafer to a temperature greater than about 500 °C. Nevertheless, the nitrogen contamination problem must be overcome before detailed studies of interface bonding using a N_2O source gas can be definitive with respect to any preferential nitrogen atom incorporation at the SiC–SiO_2 interface. It should be further noted that the SiC samples used in this study were n-type with a N atom doping level of $\sim 1.4 \times 10^{18}$ cm^{-3}, so that the N contamination may have its origin in the doping of the SiC wafers. However, it cannot be attributed simply to the doping because the area density of dopant atoms in a 2 nm thickness ($\sim$2 electron escape depths) is 3×10^{11} cm^{-2}, which is considerably less than the minimum AES detection limit of 10^{13} cm^{-2}. In spite of the sub-monolayer surface N concentration, information relative to oxidation rates could be obtained using the N_2O source gas. In the case of Si, as-loaded samples generally showed small levels of oxygen contamination, but never showed any nitrogen signal, so that more detailed interface bonding studies could be performed with both O_2 and N_2O source gases [43]. Prior to oxidation, the flat and vicinal SiC wafers displayed essentially the same (63%) Si/C surface ratios so that changes in these ratios could be correlated with the effects of the oxidation processes. As the oxidation time for the SiC wafers is increased, there are four changes evident in the SiC spectra in figures 15(a) and (b): (i) the lineshapes and multiplicity of features within the Si_{LVV} group changed, (ii) the C_{KVV} signal strength decreased, (iii) the N_{KLL} signal strength decreased and (iv) the O_{KVV} signal strength increased.

These spectral changes are consistent with the growth of a SiO_2 film on the SiC substrate. Figures 14(a) and (b) and 15(a) and (b) display, respectively, changes in (a) the Si_{LVV} and (b) the C_{KVV} (AES) features as a function of the oxidation time for flat (figure 14) and vicinal (figure 15) surfaces. Consider first the Si_{LVV} features in figures 14(a) and 15(a). The feature at $\sim$88 eV is associated with Si–C bonds, in particular with a Si atom that is bonded to four C atoms. As the oxidation proceeds this feature decreases in strength as the Si–O feature at $\sim$76 eV increases. These changes in relative intensity are due to increases of the oxide thickness with time and are consistent with the relative values of the electron escape depth, $\sim$0.6 nm, and the oxide thickness. There is also a shift of the Si–C feature to lower energy as the oxidation proceeds; this is more easily seen in the spectra for the off-axis sample. Figures 16(a) and (b) display the integrated Si_{LVV} spectra. It is evident from figures 14(a) and 16(a) that, as the intensity of the Si–C feature decreases, the position of this spectral feature moves to lower energy. In particular, in figure 14(a), the Si–C feature is evident as a distinct spectral peak at $\sim$88 eV prior to oxidation. After the oxidation has progressed for 3 min it has shifted to lower energy and appears as a shoulder at $\sim$84 on the 76 eV peak. In contrast, the C–Si feature in the C_{KVV} spectrum in figure 15(a) simply decreases in strength as the oxidation process proceeds. The absence of any significant spectral change in this region of the AES spectrum is indicative of the fact that C–O bonds are not formed during the RPAO process.

The development of interfacial C–O bonds would produce a satellite peak at lower energy, which would increase in relative strength to the C–Si feature as the oxide growth proceeds and the AES signal becomes more sensitive to the SiC interface than the bulk. The oxide thickness can be obtained to 65% from the relative intensity changes in the C_{KVV} feature using

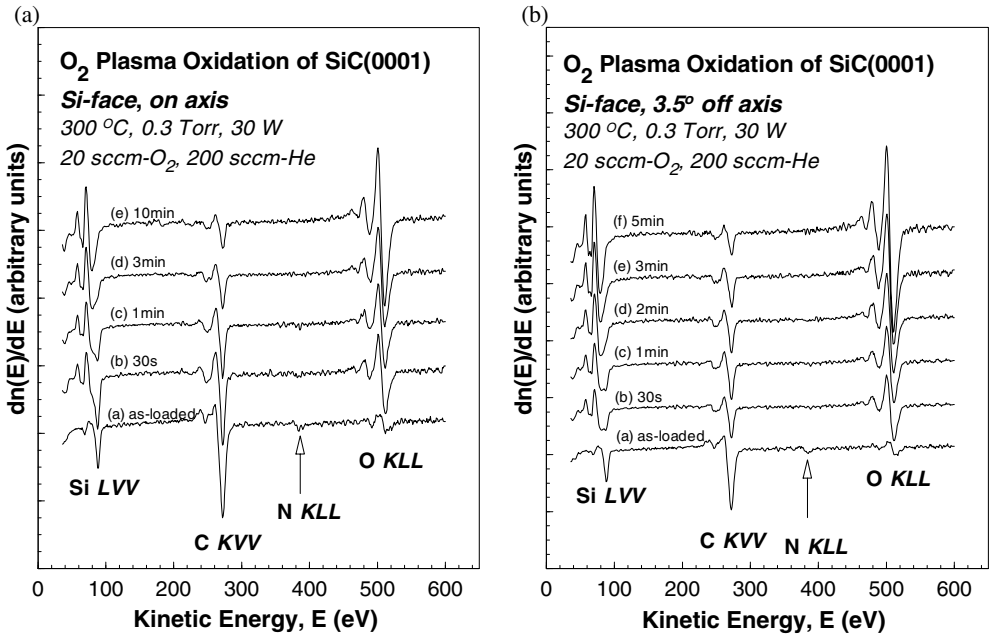

Figure 14. Derivative mode AES spectra for (a) flat and (b) vicinal SiC with Si-atom terrace terminations obtained by RPAO at 300 °C using O_2 as the oxygen atom source gas.

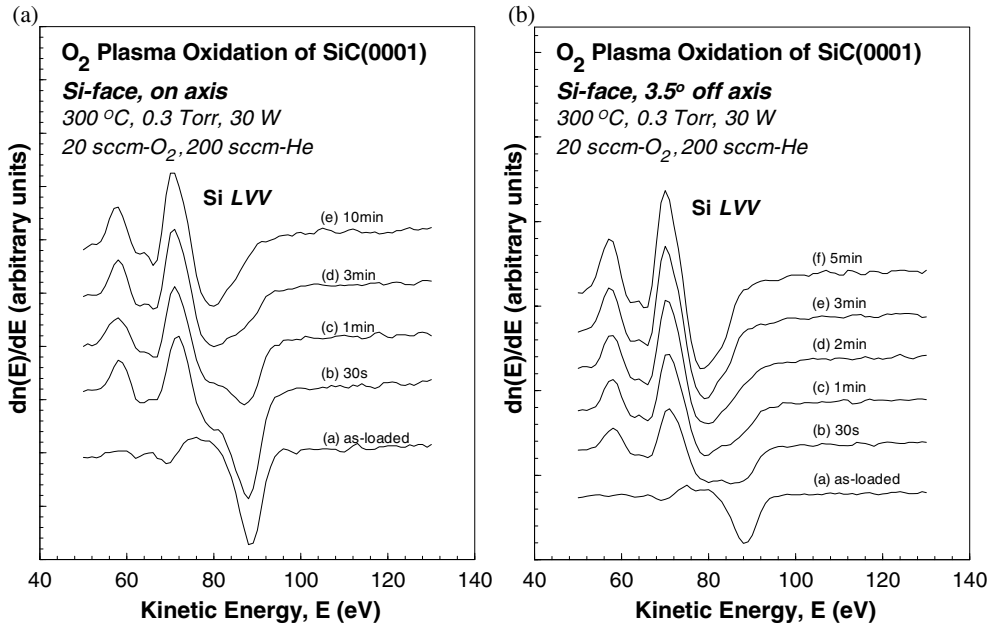

Figure 15. Changes in the Si_{LVV} AES features as a function of the oxidation time for (a) flat and (b) vicinal SiC surfaces with Si-atom terrace terminations for O_2 RPAO.

the characteristic escape depth of ∼0.96 nm for 275 eV electrons. A similar approach has been applied for the determination of the oxide thickness for the RPAO process on Si and has been

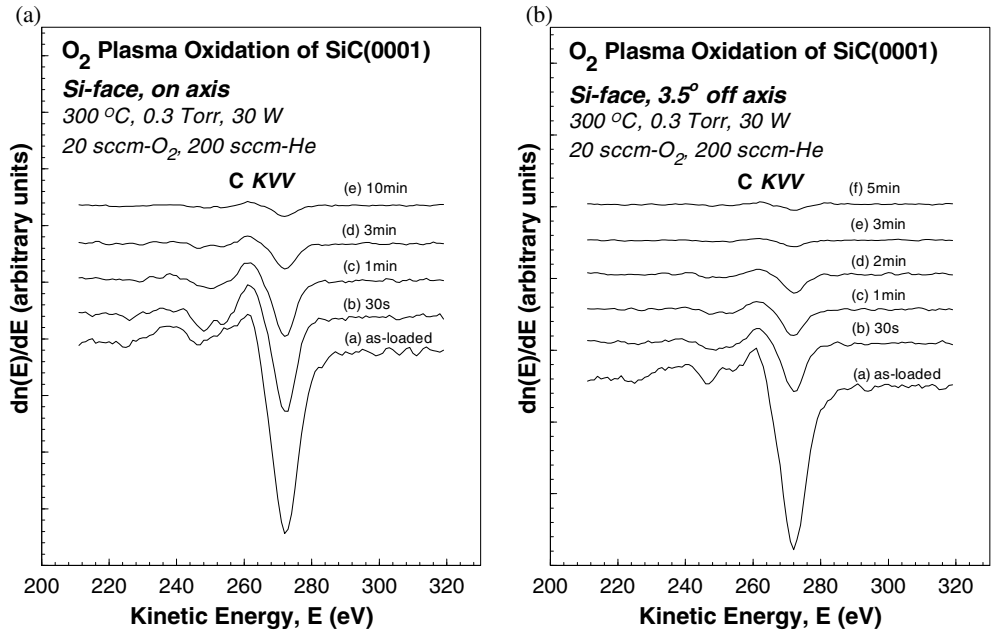

Figure 16. Changes in the C_{KVV} AES features as a function of the oxidation time for (a) flat and (b) vicinal SiC surfaces with Si-atom terrace terminations for O_2 RPAO.

validated by a direct measurement of oxide thickness by cross-sectional HRTEM. Figures 17(a) and (b) show log–log plots, respectively, of the oxide thickness versus the oxidation time for the RPAO of (a) Si and (b) SiC for the O_2 source gas. In each instance the data can be fitted by a power law dependence of the form $t_{ox} = at^b$, where t_{ox} is the oxide thickness in nanometres, t is the oxidation time in minutes and a and b are fitting parameters [43, 44]. The initial oxidation rates are about one and one-half times faster for the vicinal than for the flat wafers and the initial oxidation rates are faster for Si than for SiC. However, the power law exponents for the SiC oxidations for both flat and vicinal surfaces are greater than the corresponding exponential factor for Si. However, all of these power law exponents are less than 1. The relative differences in the power law factors means that, at long times of about 10 min or more, the thicknesses of the oxides formed on both Si and SiC are comparable for both the flat and vicinal wafers. Figure 18 illustrates this by showing a comparison of oxide thickness versus oxidation time for flat Si and SiC; a similar situation also prevails for the oxidation of the off-axis wafers. Finally for the RPAO of Si using the same relative flow rates of N_2O and O_2, the oxide growth rate was slower by a factor of two using the N_2O source gas [43]. Comparisons of RPAO rates have also been made for SiC for plasma excited O_2 and N_2O source gases. For the same relative flow rates of these two source gases, the situation is reversed with respect to Si, i.e. the oxidation rate of SiC is greater using the N_2O source gas. This increased growth rate using plasma excited species from the N_2O discharge is illustrated in figure 20 for the RPAO of flat SiC wafers.

All of the results presented above have been for SiC wafers with Si-terminated surfaces. Studies have also been made of flat and off-axis wafers with C-terminated surfaces. In this case the terminating atoms on the flat surfaces and terraces between the step edges are C and those at the set edges are Si. AES traces have been analysed and the kinetics have been studied as well. Figures 21(a), (b) and 22(a), (b) are, respectively, derivative AES spectra for Si_{LVV} flat and 3.5°

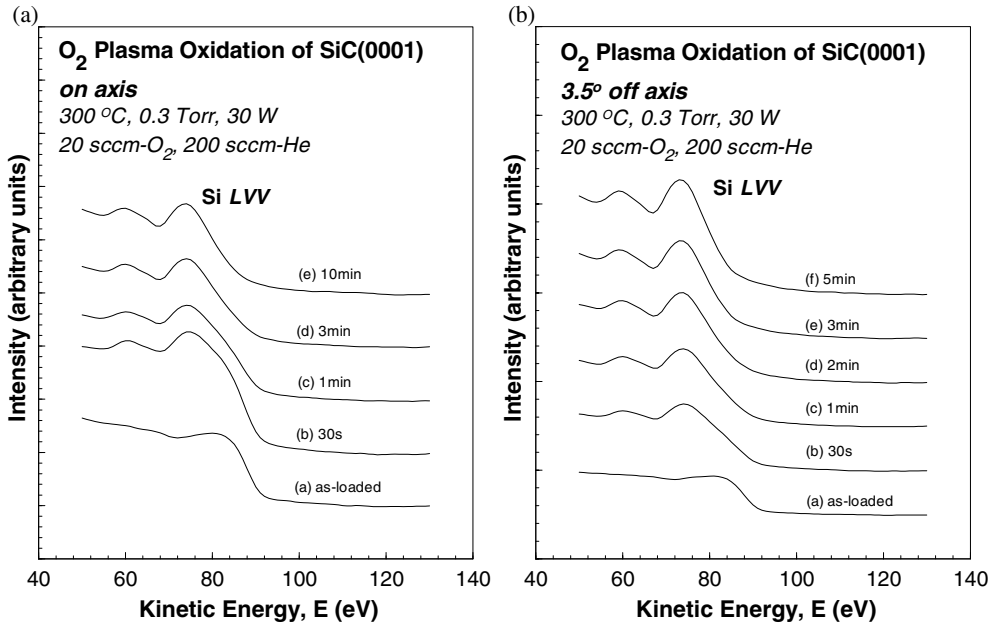

Figure 17. Integrated Si_{LVV} AES spectra as a function of the O_2 RPAO oxidation time for (a) flat and (b) vicinal SiC surfaces with Si-atom terrace terminations.

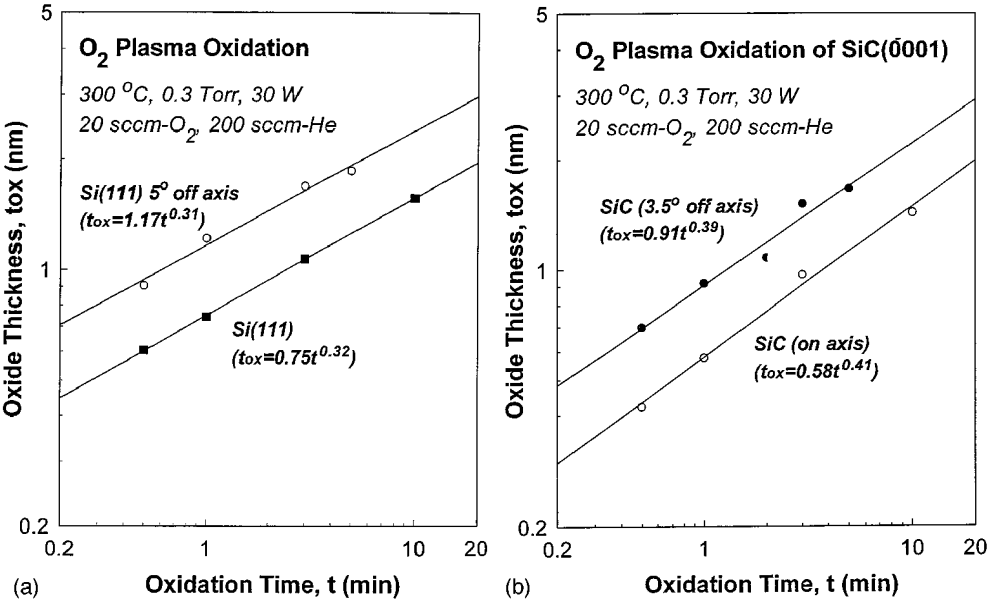

Figure 18. Log–log plots of the oxide thickness versus oxidation time for the O_2 RPAO of flat and vicinal (a) Si and (b) SiC with Si-atom terrace terminations. The data are fitted to a power law dependence, $t_{ox} = at^b$.

off axis, and C_{KVV} flat and 3.5° off axis, C-atom-terminated SiC(0001) surfaces subjected to the RPAO process. These spectra are the C-face analogues to the spectra in figures 15(a), (b) and 16(a), (b).

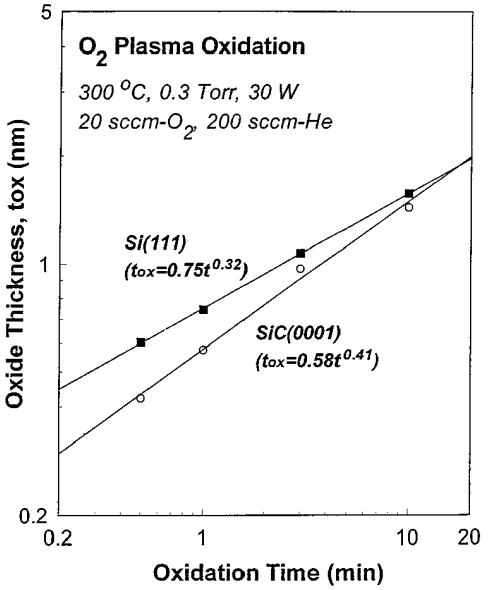

Figure 19. Log–log plots comparing oxide thickness versus oxidation time for the O_2 RPAO of flat Si and SiC with Si-atom terrace terminations. The data are fitted to a power law dependence, $t_{ox} = at^b$.

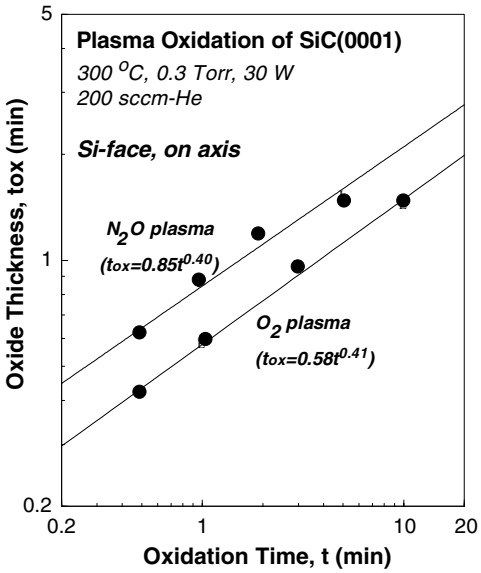

Figure 20. Log–log plots comparing the oxide thickness versus oxidation time for the RPAO of flat SiC with Si-atom terrace terminations using O_2 and N_2O as the oxygen atom source gases. The data are fitted to a power law dependence, $t_{ox} = at^b$.

Table 1. Oxidation rates for flat and vicinal Si and 6H SiC with Si and C faces.

Wafer surface	Comparative oxidation rate ($R_{vicinal}/R_{flat}$)
(a) Oxidation of Si(111)	
Si face	1.56 (5° off set)
	1.39 (scaled to 3.5° off set)
(b) Oxidation of SiC(0001)	
6H SiC Si face	1.57 (3.5° off set)
6H SiC C face	1.12 (3.5° off set)
Comparative oxidation rates for SiC ($R_{C\text{-face}}/R_{Si\text{-face}}$)	
Flat faces	1.16
Vicinal faces[a]	0.82

[a] C faces have Si atoms at step edges, while Si faces have C atoms at step edges.

Table 1 includes oxidation rate comparisons for (i) flat and vicinal Si(111) and (ii) flat and vicinal 6H SiC(001) with Si and C faces. Oxidation rates for vicinal wafers are generally faster than for flat wafers with the same surface termination. For the Si(111) wafers the increased oxidation rate for the vicinal samples off-cut $\sim$5° in the 112 direction is 1.6. If it is assumed that increases in oxidation are proportional to the number surface steps/cm, which for angles $<$10, is also proportional to the off-cut angle, then the increased rate scaled down for a 3.5° off-cut angle is $\sim$1.4. For the 6H SiC(0001) wafers, the increased rates of oxidation for vicinal as compared to flat wafers are 1.6 for Si faces and 1.1 for C faces. The oxidation rate of flat SiC with a C face is about 1.2 times larger than for SiC with a Si face. However, the oxidation

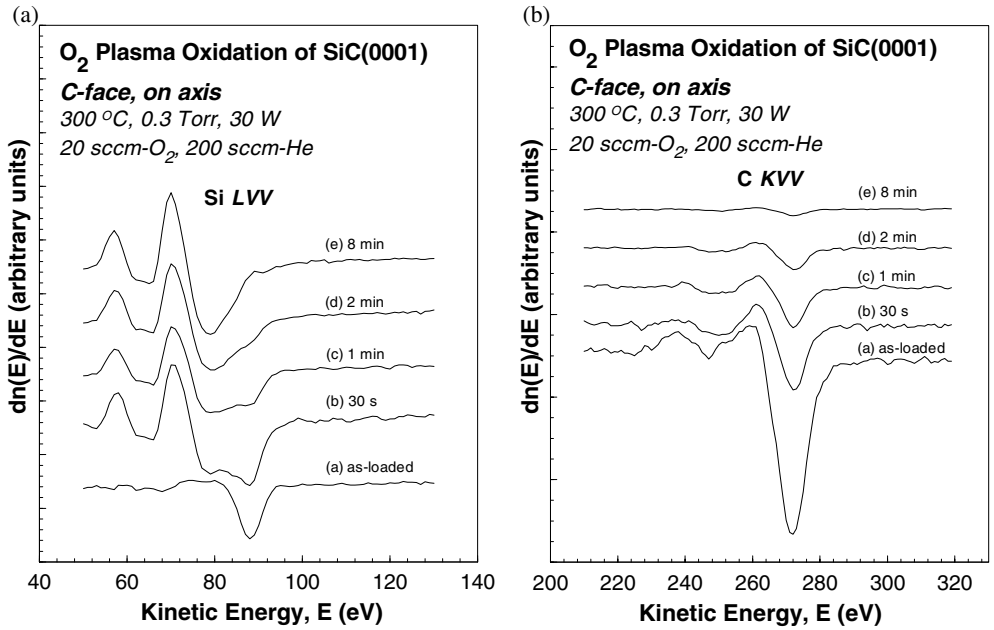

Figure 21. Changes in the Si_{LVV} AES features as a function of the oxidation time for (a) flat and (b) vicinal SiC surfaces with C-atom terrace terminations for O_2 RPAO.

for vicinal SiC with a C face is slower than that of SiC with a Si face by a factor of 0.82. These results are consistent with faces and edges terminated with C atoms always showing faster oxidation than for the corresponding face and edge terminations with Si atoms. Finally, the comparison between the oxidation rates of Si(111) and SiC(0001) is not as straightforward because of the different values of t_{ox} as discussed above, i.e. the ratio of rates is time-dependent.

3.3. Discussion and summary for remote plasma oxidation

3.3.1. AES results. The analysis of the AES spectra for the flat and vicinal SiC surface RPAO processes using the O_2 source gas indicates:

(i) the solid state oxidation product is SiO_2;
(ii) there are no detectable interfacial C–O bonds;
(iii) for Si-terminated surfaces oxidation proceeds initially more rapidly on vicinal surfaces than on flat surfaces, paralleling what has been found for Si, whereas for C-terminated surfaces the reverse is true.

The primary solid state oxidation product for thermal oxidation of SiC is also SiO_2; however, there have been reports of the observation of C–O at or near the SiC–SiO_2 interface prepared by thermal oxidation [14]. This means that there are significant differences in the oxide formation chemistries by low temperature plasma-assisted and high temperature thermal oxidation processes. For example, in the plasma-assisted processes the oxidation species are typically long-lived molecular metastables, such as O_2^*, or positive molecular ions, such as O_2 [17], whereas in the thermal oxidation process the oxidation species are typically O atoms. Since the thermal and plasma oxidation processes are qualitatively different with respect to the formation of C–O bonds, then the differences between the two types of oxidation

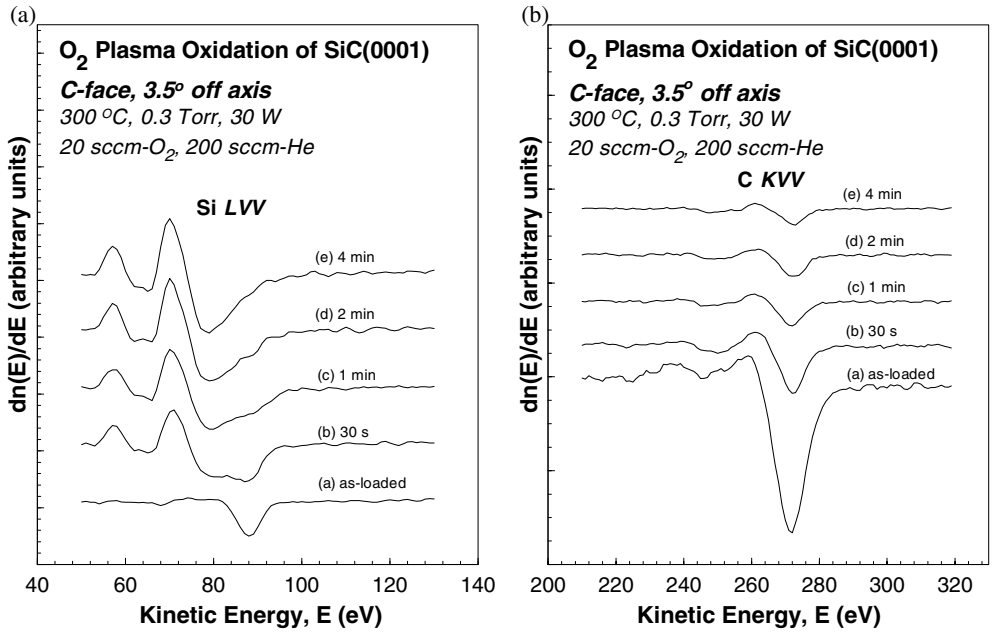

Figure 22. Changes in the C_{KVV} AES features as a function of the oxidation time for (a) flat and (b) vicinal SiC surfaces with C-atom terrace terminations for O_2 RPAO.

processes could be expected to require different post-oxidation and post-deposition procedures for forming low defect density SiC–SiO_2 interfaces. However, this is not the case, as is discussed in section 4 of this paper.

Before discussing this aspect of the experimental results, additional aspects of the power law fits are discussed below. The power law fits to RPAO data show that the oxidation process proceeds very rapidly initially and then slows down considerably with increasing oxidation time. This means chemical reaction rates between excited oxygen species and Si- and C-atom dangling bonds on Si and SiC, respectively, are decreased after Si–O bonds and a superficial layer of SiO_2 are formed at the onset of RPAO [45]. This is the case for both Si- and C-atom-terminated surfaces.

Differences between the oxidation rates of flat and vicinal wafers of 6H SiC with both Si- and C-atom terminations are presented in table 1. Significant differences between oxidation rates between flat and vicinal wafers indicate different modes of oxidation. For example, if the oxidation rate for vicinal wafers is greater than for flat wafers, as for 6H SiC with a Si face and for Si(111), then the modes of oxidation of the flat and vicinal wafers are different. When this difference is large, the oxidation of the flat wafers proceeds in a direction normal to the wafer surface, whereas the oxidation of the vicinal wafers proceeds in a direction parallel to the step surfaces. On a microscopic scale, this means that the step edge atoms of the vicinal surfaces of Si(111) (Si atoms), and 6H SiC with a Si face (C atoms), have a higher reaction rate with the activated plasma-activated oxygen species than the surface atoms. The oxidation rates of flat and vicinal 6H SiC with C faces are not significantly different (see table 1). This means that surface C atoms are oxidized more effectively than step edge Si atoms.

For the case of RPAO of Si the oxidation rate for flat surfaces is faster using O_2 than N_2O for the same relative flow rates of He and O_2 or N_2O. For the RPAO of SiC on Si surfaces the situation is reversed for flat surfaces and the oxidation rate is faster using N_2O. A model

has been proposed for RPAO of Si that explains the differences in the oxidation rates using O_2 or N_2O source gases [46]. This model was developed primarily to explain the retention of nitrogen atoms at the Si–SiO_2 interface during oxide growth using the N_2O source gas. The surface contamination of SiC by nitrogen makes it impossible to determine whether there is nitrogen retention at the SiC–SiO_2 interface during oxide growth in N_2O. This issue requires additional study.

3.3.2. Electrical properties of SiC–SiO_2 interfaces. This section summarizes results of recent electrical measurements made on MOS capacitors, in particular it compares values of D_{it} as extracted from capacitance–voltage measurements on SiC interfaces prepared on p-type substrates and employed off-axis wafers with Si surface terminations. The experimental studies of Stein von Kaminski *et al* [42] have demonstrated mid-gap D_{it} values in the low 10^{11} cm^{-2} eV^{-1} range for interfaces prepared by high temperature thermal oxidation. These device structures used metal electrodes. The attainment of low defect densities required two annealing steps: (i) a post-oxidation Ar/H_2 mixture at 1150 °C and (ii) a conventional PMA in an H_2 containing ambient at 400 °C after metallization. When annealing procedures that did not include H_2 in the 1150 °C anneal were applied to the RPAO-formed interfaces, the D_{it} values were significantly higher, in the 10^{13} cm^{-2} eV^{-1} range [42]. However, as shown in [27], these D_{it} values were significantly reduced for the RPAO interfaces following a high temperature (1150 °C) anneal in an Ar/H_2 mixture. It is interesting to note that the difference in D_{it} values between RPAO devices subjected to the Ar and Ar/H_2 anneals is very nearly equal to the density of carbon atom dangling bonds at the step edges. This suggests the possibility that carbon atom dangling bonds are not terminated during the oxidation or oxide deposition steps, or during the conventional PMA. Consider first the RPAO interfaces. Since our studies show no C–O bonding in interfacial regions for either the flat or vicinal wafers, it is suggested that the step edge carbon atom dangling bonds may remain unterminated after the oxidation process. The high defect density after conventional 400 °C PMA in a hydrogen-containing ambient further suggests that the step edge carbon atom dangling bonds are not hydrogen-terminated by this process. If this is the case then hydrogen atom production during the 1150 °C anneal in Ar/H_2 is sufficiently high to produce C–H bonding at the step edges. Since thermal oxidation processes show evidence for C–O bonding in interfacial transition regions [14] and the RPAO process does not, this suggests that there might be differences related to the way step carbon atom dangling bonds are terminated, either during thermal and plasma oxidations, or in post-oxidation annealing. However, this appears not to be the case, since interfaces produced by high temperature thermal oxidation also require a high temperature anneal in an H_2-containing ambient. This means that, even though C–O bonds can be found in silicon oxycarbide transition regions after high temperature thermal oxidation [3], they may not be formed in sufficient numbers at carbon atom step edges to neutralize dangling bond defects. Alternatively, the local bonding environment of carbon atoms in interfacial regions and at the Si–C step edges is different and may be a contributing factor to oxygen atom termination. Finally, it is also interesting to note that fabrication of low D_{it} interfaces on n-type SiC by RPAO and thermal oxidation does not require a high temperature anneal in an H_2-containing ambient [26]. There are two possible explanations for not requiring such an anneal for the RPAO-formed interfaces:

(i) the active interfacial defects are in the bottom half of the SiC bandgap and hence are more active in p-type material, or
(ii) the formation of C–O bonds at an SiC interface is Fermi-level-dependent favouring C–O bond formation in n-type material.

The wafers that we studied were nitrogen doped n-type wafers and there was no evidence of interfacial C–O bond formation. However, the concentration of step edge C atom dangling bonds that are available for termination by C–O bonding is below the AES detection limit. It is clear that these questions identified with respect to electrical results on SiC devices need additional experimental and theoretical studies before they can be satisfactorily resolved. In particular, electron spin resonance experiments that can readily distinguish between Si and C atom dangling bonds may be helpful in resolving the issues discussed above.

4. Summary

The objective in this paper is first to identify and then understand differences between high temperature thermal and low temperature remote plasma-assisted oxidation of SiC and relate this to device performance. The first section of the paper has addressed the thermo-chemical stability of interfacial silicon oxycarbide regions (Si, C)O_x that have been identified at interfaces between Si and thermally grown oxides. This portion of the study has demonstrated that these regions are formed at high temperatures, $\sim$950 °C, but additionally that they dissociate at higher temperatures, $\sim$1050 °C. This thermo-chemical behaviour is consistent with the improved performance of SiC devices in which thermal oxidation is performed at temperatures of at least 1050 °C. Post-oxidation annealing at 900 °C then optimizes interfacial bonding in Si suboxide regions.

This paper has presented a detailed study of the chemical bonding changes and kinetics of remote plasma-assisted oxidation at interfaces with flat and off-axis 6H SiC(0001) with Si- and C-atom-terminated surfaces. These results have been compared with RPAO of flat and off-cut Si(111). Differences in etch rates between flat and off-cut SiC have been identified for both species of surface-terminating atoms. These studies have included initial studies of RPAO processes in which N_2O is substituted for O_2 in the source gas mix. The behaviours for Si and SiC are significantly different.

Electrical measurements have been focused on interfacial defects and have provided important insights into differences between interfacial defects in Si devices prepared on off-axis Si(111) and in SiC devices with off-axis SiC(0001) with Si-atom terminations. In the Si devices the terrace and step edge atoms are Si, whilst in the SiC devices those terrace atoms are Si and the step edge atoms are C.

Finally, there has been much recent interest in interface nitridation, particularly in devices prepared on 4H SiC [47, 48]. Nitridation has improved channel mobilities in NMOS devices. This presents an interesting research change for remote plasma processing which we are currently addressing in our research group.

Acknowledgments

This research has been supported by the Office of Naval Research and Air Force Office of Scientific Research under two research grants, one to North Carolina State University, and the second a MURI grant to Vanderbilt University, with North Carolina State University as sub-contractor.

References

[1] Grunthaner F J and Grunthaner P J 1986 *Mater. Sci. Rep.* **1** 69
[2] Halbritter J 1988 *J. Mater. Res.* **3** 506
[3] Hattori T 1995 *CRC Crit. Rev. Solid State Mater. Sci.* **20** 339

[4] Kiester J W, Rowe J E, Kododzie J J, Niimi H, Tao H-S, Madey T E and Lucovsky G 1999 *J. Vac. Sci. Technol.* A **17** 1250
[5] Chen X and Gibson J M 1997 *Appl. Phys. Lett.* **70** 1462
[6] Lucovsky G, Banerjee A, Niimi H, Koh K, Hinds B, Meyer C, Lüpke G and Kurz H 1997 *Appl. Surf. Sci.* **117** 202
[7] Choi W K, Poon F W, Loh F C and Tan K L 1997 *J. Appl. Phys.* **81** 7386
[8] Ishikawa K, Uchiyama Y, Ogawa H and Fujimura S 1997 *Appl. Surf. Sci.* **117** 212
[9] Yasuda N, Takagi S and Toriumi A 1997 *Appl. Surf. Sci.* **117** 216
[10] Awaji N, Ohkubo S, Nakanishi T, Takasaki K and Komiya S 1997 *Appl. Surf. Sci.* **117** 221
[11] Toriumi A, Satake H, Yasuda N and Tanamoto T 1997 *Appl. Surf. Sci.* **117** 230
[12] Sakoda T, Matsumura M and Nishioka Y 1997 *Appl. Surf. Sci.* **117** 241
[13] Lucovsky G, Banerjee A, Hinds B, Claflin B, Koh K and Yang H 1997 *J. Vac. Sci. Technol.* B **15** 1074
[14] Hornetz B, Michel H-J and Halbritter J 1994 *J. Mater. Res.* **9** 3088
[15] Chaudrhy M I 1989 *J. Mater. Res.* **4** 404
[16] Onneby C and Pantano C G 1997 *J. Vac. Sci. Technol.* A **15** 1597
[17] Lipkin L and Palmour J W 1996 *J. Electron. Mater.* **25** 909
[18] Luthra K I 1991 *J. Am. Ceram. Soc.* **74** 1095
[19] Tsu D V, Lucovsky G and Davidson B N 1989 *Phys. Rev.* B **40** 1795
[20] Hinds B J, Wang F, Wolfe D M, Hinkle C L and Lucovsky G 1998 *J. Non-Cryst. Solids* **227** 507
[21] Lucovsky G 1998 *J. Non-Cryst. Solids* **227** 1
[22] Ouisse T 1996 *Phil. Mag.* B **73** 325
[23] Fitch J T, Kobeda E, Lucovsky G and Irene E A 1989 *J. Vac. Sci. Technol.* B **7** 153
[24] Yasuda T, Ma Y, Habermehl S and Lucovsky G 1992 *Appl. Phys. Lett.* **60** 434
[25] Lucovsky G, Ma Yi, Hattangady S V, Lee D R, Lu Z, Misra V, Wortman J J and Whitten J L 1994 *Japan. J. Appl. Phys.* **33** 7061
[26] Lucovsky G, Banerjee A, Hinds B, Claflin B, Koh K and Yang H 1997 *J. Vac. Sci. Technol.* B **15** 1075
[27] Goelz A, Janssen R, Stein von Kamienski E and Kurz H 1996 *The Physics and Chemistry of SiO_2 and the Si–SiO_2 Interface* ed H Z Massoud, E H Poindexter and C R Helms (Pennington, NJ: Electrochemical Society) p 753
[28] Bjorkman C H, Shearon C E Jr, Ma Y, Yasuda T, Lucovsky G, Emmerichs U, Meyer C, Leo K and Kurz H 1993 *J. Vac. Sci. Technol.* B **11** 964
[29] Yasuda T, Lee D R, Bjorkman C H, Ma Y, Emmerichs U, Meyer C, Leo K and Kurz H 1993 *Mater. Res. Soc. Symp. Proc.* **315** 375
[30] Lucovsky G, Tsu D V, Rudder R A and Markunas R J 1991 *Thin Film Processes* ed J L Vossen and W Kern (San Diego, CA: Academic) pp 565–619
[31] Wolfe D M, Wang F, Hinds B J and Lucovsky G 1998 *Mater. Res. Soc. Symp. Proc.* **483** 203
[32] Lucovsky G, Yang J, Chao S S, Tyler J E and Czubatyj W 1983 *Phys. Rev.* B **28** 3224
[33] Socrates G 1994 *Infrared Characteristic Group Frequencies* 2nd edn (Chichester: Wiley) chapter 18
[34] Reubel H, Schroeder B, Fuhs W, Krauskopf J, Rupp T and Bethge K 1987 *Phys. Status Solidi* b **139** 131
[35] Feldman D W, Parker J H Jr, Choyke W J and Patrick L 1968 *Phys. Rev.* **173** 787
[36] Bellamy L J 1975 *The Infrared Spectra of Complex Molecules* (London: Chapman and Hall) chapter 20
[37] Smith A L 1991 *The Analytical Chemistry of Silicones* (New York: Wiley) p 336
[38] Hollinger G and Himpsel F J 1984 *Appl. Phys. Lett.* **44** 93
[39] Grunthaner P J, Hecht M H, Grunthaner F J and Johnson N M 1987 *J. Appl. Phys.* **61** 629
[40] Zhang H and Pantano C G 1990 *J. Am. Ceram. Soc.* **73** 958
[41] Soraru G D, D'Andrea G, Campostrini R, Babonneau F and Mariotto G 1995 *J. Am. Ceram. Soc.* **78** 379
[42] Stein von Kaminski E *et al* 1995 *Microelectron. Eng.* **28** 201
[43] Lucovsky G, Niimi H, Koh K, Lee D R and Jing Z 1996 *The Physics and Chemistry of SiO_2 and the Si–SiO_2 Interface* ed H Z Massoud, E H Poindexter and C R Helms (Pennington, NJ: Electrochemical Society) p 441
[44] Wolters D R and Zegers-van Duynhoven A T A 1989 *J. Appl. Phys.* **65** 5126
[45] Thanikasalam P, Whidden T K and Ferry D K 1996 *J. Vac. Sci. Technol.* B **14** 2840
[46] Koh K, Niimi H and Lucovsky G 1996 *Mater. Res. Soc. Symp. Proc.* **429** 233
[47] McDonald K, Weller R A, Pantelides S T, Feldman L C, Chung C Y, Tin C C and Williams J R Jr 2003 *J. Appl. Phys.* **93** 2719
[48] McDonald K, Feldman L C, Weller R A, Chung C Y, Tin C C and Williams J R 2003 *J. Appl. Phys.* **93** 2257